Tri-Needle Coaxial Electrospray Engineering of Magnetic Polymer Yolk-Shell Particles Possessing Dual-Imaging Modality, Multi-Agent Compartments and Trigger Release Potential

Chunchen Zhang [†, ‡], *Zhi-Cheng Yao* [†, ‡], *Qiuping Ding* [§], *James J Choi* [⊥], *Zeeshan Ahmad* [//], *Ming-Wei Chang* [†, ‡, *], *Jing-Song Li* [†]

[†]Key Laboratory for Biomedical Engineering of Education Ministry of China, Hangzhou, 310027, PR China

[‡]Zhejiang Provincial Key Laboratory of Cardio-Cerebral Vascular Detection Technology and Medicinal Effectiveness Appraisal, Hangzhou, 310027, PR China

[§]Department of Biomedical Engineering, College of Biomedical Engineering and Instrument Science, Zhejiang University, Hangzhou, 310027, PR China

[⊥]Bioengineering Department, Imperial College London, London SW7 2BP, UK

[//]Leicester School of Pharmacy, De Montfort University, The Gateway, Leicester, LE1 9BH, UK

ABSTRACT:

Particulate platforms capable of delivering multiple actives while providing diagnostic features have gained considerable interest over the last few years. In this study, magnetic polymer yolk-shell particles (YSPs) were engineered using a tri-needle coaxial electrospraying technique enabling dual-mode (ultrasonic and magnetic resonance) imaging capability with specific multi-drug compartments *via* an advanced single-step encapsulation process. YSPs comprised magnetic Fe_3O_4 nanoparticles (MNPs) embedded in the polymeric shell, an interfacing oil layer and a polymeric core (i.e. composite shell-oil interface-polymeric core). Ultrasound backscatter signal frequency was modulated through YSP loading dosage, and both T_1 and T_2 weighted MRI signal intensities were shown to reduce with increasing MNP content (YSP outer shell). Three fluorescent dyes (selected as model probes with varying hydrophobicities) were co-encapsulated separately to confirm YSP structure. Probe release profiles were tuned by varying power or frequency of an external auxillary magnetic field (AMF, 0.7 mT (LAMF) or 1.4 mT (HAMF)). In addition, an "inversion" phenomenon for AMF-enhanced drug release process was captured and is reported. Low YSP cytotoxicity (5mg/ml) and biocompatibility (murine, L929) was confirmed. In summary, magnetic YSPs demonstrate timely potential as multifunctional theranostic agents for dual-imaging modality and magnetically controlled co-active delivery.

KEYWORDS: York-shell particles, dual-imaging modality, multi-drug release, electrospray, controlled release, auxiliary magnetic field

1. INTRODUCTION

Particles exhibiting combined diagnostic (e.g. imaging) and therapeutic (controlled or triggered active release) functions are extremely valuable to address several global healthcare challenges; with extensive recent efforts focusing on tumor targetting, personalized medicine and biomedical engineering.[1-2] Such particles enable a single carrier system to provide real-time disease diagnosis *in-vivo* as well as fine-tune active release at a specific location in timely fashion. This multi-faceted approach, *in lieu*, has propelled them as emerging paradigms for clinical practice.[3-5] Furthermore, the functionality of such particles goes beyond image-guided drug delivery; in that rapid assessment and treatment of disease is accomplished at an early stage whilst minimizing unwanted cytotoxic side-effects often arising from conventional strategies.[6-7]

Magnetic resonance imaging (MRI) is a pain-free and safe diagnostic procedure that has numerous advantages over other routine imaging methods including excellent anatomic detail, exquisite soft tissue contrast, high spatial resolution and multi-planar imaging capacity.[8-9] MRI signal is dependent on longitudinal (T_1) and transverse (T_2) proton relaxation times of water (mainly) and therefore; differences arising in these values provide variable contrast in images. MRI contrast agents are able to decrease T_1 and T_2 relaxation times, and subsequently improve contrast between normal and diseased tissues.[10-11] Furthermore, because of their interaction with magnetic fields, contrast agents have also been used to control active agent release from co-encapsulated or co-embedded systems *via* an auxiliary magnetic field (AMF).[12] In contrast, ultrasound (US) is a well-established and widely used clinical imaging modality. This technique provides real time imaging, particularly for blood flow, and several advantages relating to cost effectiveness, portability and high patient acceptability have led to its preference (globally) in various clinical settings.[13]

While both of these imaging modalities are essential in present and emerging diagnostic technologies, MRI and US have their own limitations. For instance, MRI is not applicable for real-time imaging and also requires a relatively longer time period for image acquisition.[9] US imaging provides lower resolution and penetration depth, which hinders its ability to discriminate between superficial and echogenic structures.[8] In this regard, the development of a dual-imaging modality technique, combining both MRI and US, will be timely and enables much needed advance from either platform. Moreover, to maximize the merits of an integrated imaging technique; design and construction of effective and viable contrast agents suitable for both modalities will be of significance.[7, 9]

In recent times, encapsulation and delivery of multiple drugs from a single dosage form platform is considered to be crucial for patient compliance and advanced therapies. For example, combination of anti-inflammatory and anti-cancer drugs in a single cargo is promising for cancer therapy since targeting inflammation, in addition to restricting replication, further reduces tumor development and progression.[14] Therefore, co-encapsulation of two or more actives has potential to deliver synergistic therapeutic effects and reduced side-effects.[15] Furthermore, the possibility to co-encapsulate hydrophilic and hydrophobic drugs in a single dosage form is ideal for drug dispersibility, active release and therapeutic impact[16]. Several co-formulation strategies become resticted due to complexities surrounded active hydrophobicity, formulation, retention and delivery.

Developments in synergistic therapies (multi-drug dosing) have yielded numerous explorations and formulations which provide multiple active delivery from a single cargo.[17-18] One such area of focus has centered on encapsulated polymeric particulate systems; with conceptual designs demonstrated in bi-layer, multi-layered and several other complex systems.[19-

[21] Among all polymeric particulate formats with compartmentalized (interior) structures, yolk-shell particles (YSPs) appear least explored although they display unique features and physical properties; including low densities, large surface areas and excellent loading capacities.[22] Limited data shows the design and development of functionalized YSP interior core and outer shell have potential to enhance drug delivery, although the vast majority of related research to date has focused on inorganic materials (including silica and carbon based).[23] In this regard, polymer based YSPs will afford improved biodegradability, biocompatibility and will also be more favorable economically. Current design and preparation of YSPs involve numerous and complex steps, elevated engineering temperatures and micron-scaled etching techniques.[23]

In this study, polymer based magnetic YSPs were engineered with the ability to host multiple probes (as model chemical agents). Complex particle engineering was achieved using tri-needle co-axial electrospraying which is a single step process. Poly(ε-caprolactone) (PCL) was selected as the matrix for both core and the shell materials because of its accepted biocompatibility and related drug permeability.[19] Silicone oil was adopted as the interfacing-layer due to its moderate viscosity.[24] In order to demonstrate co-encapsulation (in seperate compartments) and delivery, Nile blue (NB) and acridine yellow (AY) were selected as model hydrophilic probes and Sudan red G (SRG) was selected due to its hydrophobic nature. Magnetic nanoparticles (MNPs) (Fe_3O_4 ~20 nm in diameter) were encapsulated into YSPs (shell layer) to enable magnetic properties. YSP composition, interior structure, biocompatibility, dual imaging modality and controlled multi-probe release from therein (with and without an external AMF trigger) were investigated.

2. MATERIALS AND METHODS

2.1. Materials

Poly(ε-caprolactone) (M_w=4.5x10^3 g/mol) and Sudan red G were purchased from Sigma-Aldrich Ltd., St Louis,USA. Silicone oil (SLO), Fe_3O_4 (nano-spheres with diameters of ~20 nm, MNPs), Nile blue, Nile red, Sodium dodecyl sulfate (SDS) Triton X-100 were obtained from Aladdin chemistry Co., Ltd, Shanghai, China. Acridine yellow (neutral) was purchased from Shanghai Macklin Biochemical Technology Co., Ltd. Agar was obtained from Shanghai EKEAR Bio&Tech Co., Ltd. Phosphate buffer solution (PBS) and glacial acetic acid (HAc) were supplied by Sinopharm Chemical Reagent Co., Ltd, Shanghai, China. Ultrapure water was produced with a Millipore Milli-Q Reference ultrapure water purifier (Molsheim, France). Modified eagles media (MEM, Gibco) and fetal bovine serum (FBS) were obtained from Invitrogen, CA, USA. Cell Counting Kit-8 (CCK-8) was purchased from Dojindo Molecular Technologies, Inc (Kumamoto, Japan).

2.2. Fabrication of Yolk-Shell Particles (YSPs) *via* tri-needle co-axial electrospray

Figure 1a is a schematic illustration of the tri-needle coaxial electrospray system used for YSP synthesis. The nozzle system comprises a set of three stainless steel needles (into one concentrically aligned nozzle spraying cylindrical head); three syringe pumps (KD Scientific KDS100, USA), a high voltage power supply (Glassman high voltage Inc. series FC, USA) and a metallic ground ring electrode (diameter~ 5 cm). For nozzle assembly, the three stainless steel needle capillaries possessed inner and outer diameters of 2.85 mm and 2.26 mm for the outer capillary, 1.60 mm and 1.07 mm for the central capillary, and 0.50 mm and 0.31 mm for the inner capillary, respectively. Media inlets of the three capillaries were connected to the corresponding syringes using silicone tubing. The corresponding liquids were injected into capillaries by independently controlled syringe pumps. The processing nozzle was connected to the high voltage power supply and the metallic ground electrode ring was located directly below

the nozzle assembly (5 mm). The power supply was used to provide a static electric field between the outlet of nozzle assembly and the ground electrode. A CCD camera (Baumer TXG02C, Germany) was connected to image capture hardware (PC) and was used to monitor real-time jetting behavior of atomized spray (formed using the tri-needle co-axial electrospray system) for stable and near-uniform particle production. The applied voltage was maintained at 10 kV for all experiments. All YSPs were fabricated using flow rates of 10 ml/h, 2.5 ml/h and 1.6 ml/h for outer, middle and inner layers, respectively (infusion rates into capillaries). For all YSP samples, media for outer and inner layers comprised 20 w/v% PCL dissolved in HAc with pre-designated quantities of MNP and hydrophilic model probes (NB or AY). Pure SLO was selected for the central interfacing particulate layer along with hydrophobic model probe (SRG). The mass ratio of NB:PCL (outer shell), SRG:SLO (central layer) and AY:PCL (inner layer) were selected as 7.5, 2 and 12 mg/g, respectively.

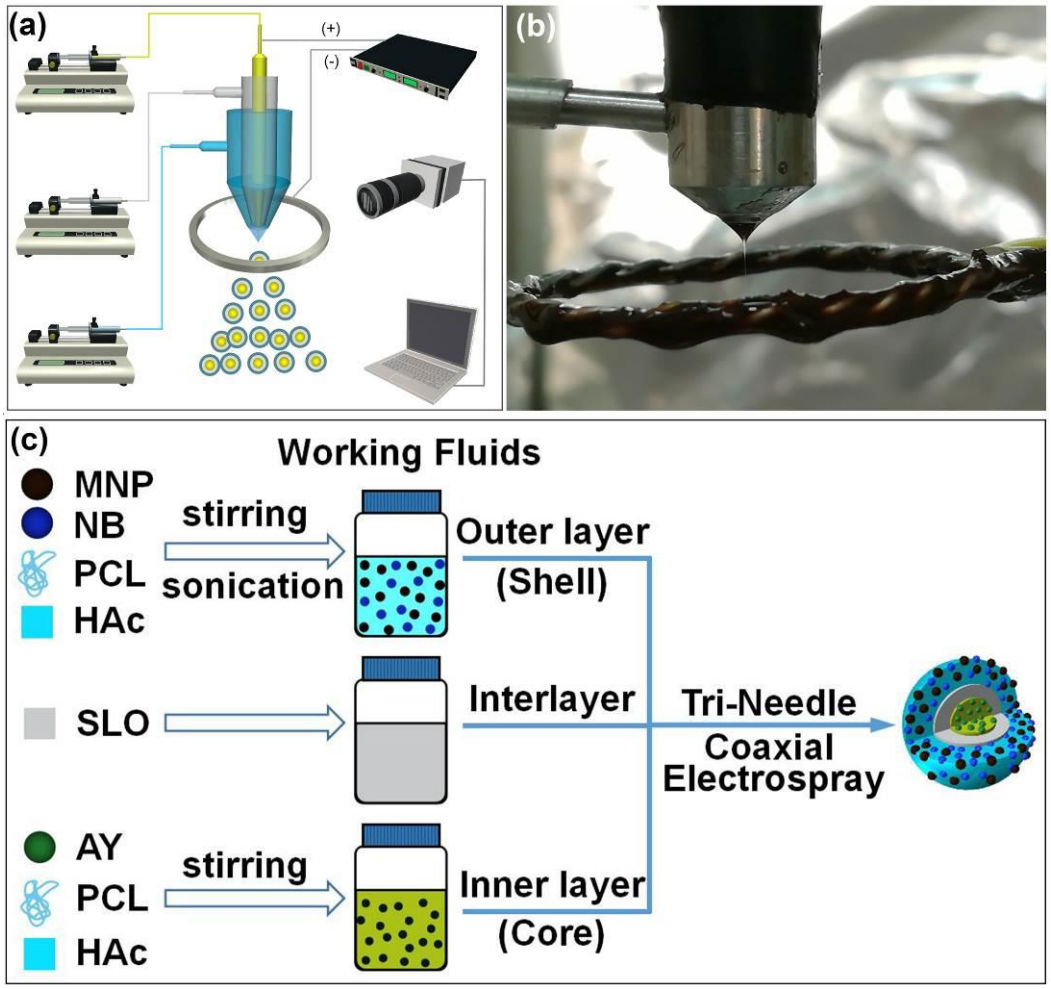

Figure 1. (a) Schematic illustration of the tri-needle coaxial electrospraying system used in this study. (b) Digital image of stable jetting behavior from the tri-needle nozzle assembly. (c) Formulation, formation and compartments of probe loaded magnetic yolk-shell particles.

2.3. Characterization

Optical, fluorescence and scanning electron microscopies (SEM) were used to observe size, surface morphology and interior structure of the YSPs. For optical and fluorescent micrographs, particles were collected directly onto microscopic glass slides and observed using an optical microscope (Pheonix BMC503-ICCF, China) and an inverted fluorescence microscope (Nikon,

Ti-S, Japan), respectively. For SEM analysis, YSPs were sprayed on aluminium film and then mounted on to a metallic stud using double-sided conductive tape for sputter coating. A thin layer of gold under vacuum (Ion Sputter MC 1000, Hitachi, Japan) was deposited for 90s. SEM images were obtained using a field emission-scanning electron microscope (FE-SEM, FEI Quanta 650 FEG, Hillsboro, Oregon, USA). The diameters of YSPs were analyzed using imageJ software (National Institute of Health, USA) directly from electron micrographs. YSP stability was assessed in two environments; in air (i.e. storage) and in PBS. YSPs were observed for changes to their surface morphology and structure at 1, 3, 5 and 7 days using SEM.

Sample composition was determined using Fourier Transform Infra-Red (FTIR) spectroscopy. Samples were prepared by mixing 2 mg of selected particles with 200 mg of KBr medium by grinding and then compressing the resulting powder into transparent pellets (pressure of 12 MPa).[25] Pellets were then scanned with FTIR (IR Affinity 1, Shimadzu, Japan) and the spectrum was obtained at a resolution of 4 cm^{-1} ranging from 4500 to 500 cm^{-1}. Each spectrum was obtained using 20 scans. X-ray diffraction (XRD) was used to confirm successful encapsulation of MNPs in YSPs, spectra were recorded with a diffractometer (X'pert PRO, Panalytical, Netherlands) equipped with standard Cu Kα radiation source (λ = 1.5405 Å) and scanned within 2θ range of 10-90° at a step size of 0.026°. The operating voltage and current were 40 kV and 40 mA, respectively. Sample magnetization curves were obtained using a vibration sample magnetometer (VSM Mini-CFM measurement system, Cryogenic Ltd., UK) at 300K under a reciprocating altered magnetic field (-30000 to 30000 Oe), and saturation magnetization was obtained from hysteresis loops.

2.4. *In-vitro* MRI evaluation.

Imaging data was acquired using a 3 Tesla MRI scanner (Magnetom Prisma, Siemens Healthcare, Erlangen, Germany) through a 20-channel head-neck coil. MRI measurements for two experimental groups and a control sample were obtained. For the first group, phantoms contained 4 mg of particulate samples at various MNP:PCL outer layer mass ratios (0, 25, 50, 75 mg/g). The second group comprised samples with identical MNP:PCL mass ratios (0.5, 1, 2, 4 mg). 4 mg of pure MNPs were used for control experiments. For phantom preparation, 1g of agar was added to 100 ml ultrapure water and the mixture was subsequently boiled for 30s and cooled. This cycle was repeated until a homogeneous agar gel was obtained, which was then allowed to cool further in atmosphere to 40 °C. All phantoms to be used for MRI were then prepared by mixing particulate samples with 10 ml of the pre-prepared agar gel and 2 ml 5 w/v% SDS aqueous solution (to improve sample wetting and enhance phantom uniformity[26]). Sample-gel mixtures were stirred thoroughly to form a uniform suspension, and were then poured into a 15 ml centrifuge tube. Pure agar phantoms (without samples) were also fabricated for control experiments.

T_1 mapping was performed using a Siemens WIP (Working In Progress) mp2rage sequence (TR/TE=5000 ms/3.37 ms, FA1=4°, FA2=5°, TI1=700 ms, TI2=2500 ms, FOV=115×75 mm^2, acquisition matrix=192×192, slice thickness=3 mm). T_1-weighted imaging was obtained using a spin echo (SE) sequence (TR/TE=2000 ms/6.2 ms, FOV=180×180 mm^2, slice thickness=4 mm). T_2 mapping and T2-weighted imaging were performed using the multi-TE spin echo sequence (TR=2900 ms, TE=10.5, 21, 31.5, 42, 52.5, 63, 73.5, 84 ms, FOV=180×73 mm^2, FA=180°, matrix size=256×256, slice thickness=2 mm, bandwith=227 Hz/Px). T_1 and T_2 maps were automatically calculated by the system using exponential curve fitting, and mean values were

calculated in the regions of interest (ROI), selecting ~50% of total area at the cross section's center.

2.5. Acoustic characterization

The setup for acoustic experiments is shown in **Figure 2**, as utilised in a previous report.[27] Pre-weighed particles (0, 2 and 10 mg) with an outer layer MNP:PCL mass ratio of 75 mg/g were suspended using 20 ml ethanol in a plastic container (2.8 cm in diameter and 3.5 cm in depth). A 5 MHz ultrasonic transducer (1.6 cm in diameter and 3 cm in depth) was vertically submerged into the suspension (serving as both transmitter and reciever) and was connected to a pulser/receiver (5073PR, Olympus Inc., Japan). All signal data from the pulser/receiver was acquired and stored using an oscilloscope (200MHz bandwith, WaveSurfer 3024, Teledyne LeCroy, USA). Parameters for acoustic experiments were kept constant (PRF=200 Hz, Energy=2, Damping=2, Gain=20 dB) and data was processed using Matlab 2013b (The Mathworks Inc., Natick, USA).

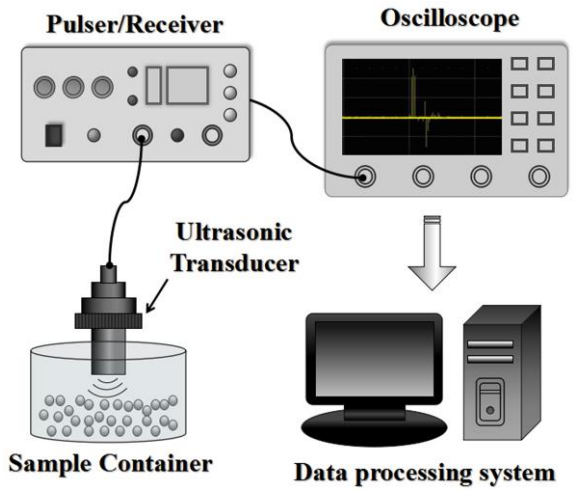

Figure 2. Acoustic experimental setup.

2.6. Probe loading capacity and encapsulation efficiency

The loading capacity (LC) of selected probes was determined as the quantity of probe encapsulated within YSPs and was calculated using **Equation 1**. The encapsulation efficiency (EE) was obtained using **Equation 2**.[28]

$$\text{LC } (\%) = \frac{\text{Weight of encapsulated probe}}{\text{Weight of YSPs}} \times 100\% \text{ , (Eqn.1)}$$

$$\text{EE } (\%) = \frac{\text{Weight of encapsulated probe}}{\text{Weight of initial added probe}} \times 100\% \text{ , (Eqn.2)}$$

2.7. *In-vitro* probe release and AMF application

Probe release profiles from various YSP layers were investigated *in vitro*. For this, 30 mg of NB and AY loaded (or alternatively SRG) YSPs were suspended using 10 mL release medium, respectively, which comprised PBS (pH=7.2) and 0.5 w/v% SDS to maintain sink conditions[29] in a 10mL glass vial. Probe release in static or AMF triggered environments at the ambient temperature (~23.5 °C) were assessed. A strong magnet was applied in close proximity to the base of sample hosting vials to completely separate YSPs from test-medium; and then 4 mL of supernatant was collected. This procedure was performed at pre-determined time intervals. Supernatant concentration was determined using UV-Vis spectroscopy (UV-2600 spectrophotometer, Shimadzu, Japan).[12] Removed analyte samples were replaced with 4 mL of fresh release medium (PBS). For AMF trigger application, a copper solenoid coil (45 turns) was laced around a plastic tube and driven by a power amplifier (HFVA-42, Foneng Science and Technology Co., Ltd., Nanjing, China). A functional signal generator (AFG1022, Tektronix, USA) was used to produce a small sinusoidal signal, which was then amplified to generate an AMF around the coiled tube. The sample hosting vial was placed in the coiled tube's hollow core,

which ensured YSPs were subjected to the applied AMF. All other conditions were constant. The effect of both frequency and power on probe release was investigated. All experiments were performed in triplicate.

In order to examine potential thermal impact (arising from AMF generation) on YSPs, a Ti32 thermal camera (Fluke Corporations, Seattle, USA) was deployed to image the process at pre-determined time intervals. Data was analyzed using SmartView software to extract temperature field distribution, which was subsequently used to calculate mean temperature.

2.8. *In vitro* cell culture and biocompatibility

YSP biocompatibility and potential cytotoxic effects were evaluated using *in vitro* cell culture. L929 mouse fibroblasts were propagated in MEM medium with 10% heat-inactivated FBS and 1% (v/v) antibiotic–antimycotic in a petri dish which were incubated at 37 °C in humidified CO_2 (5%) environment.

For biocompatibility assessement, cells were incubated for 24 h. The culture medium was replaced with 3 mL of fresh medium containing magnetic YSPs at varying concentrations (0, 1 and 5 mg/ml). For this, an YSP outer shell MNP:PCL mass ratio of 75 mg/g was selected. After 24 h, cells were visualized using fluorescent counterstaining with rhodamine-phalloidin and DAPI to observe morphology and confirm cellular state. Treated cells were washed with PBS three times and fixed with 4% paraformaldehyde for 30 min. Cell permeabilization was achieved using 0.1% Triton X-100 for 5 min followed by washing with PBS, and the procedure was carried out three times. Rhodamine-phalloidin (1:200 in PBS) was used to stain filamentous actin skeleton for 20 min and then DAPI (1:5000 in PBS) was used to stain cell nuclei for 5 min. After this, cells were imaged using inverted fluorescent microscopy.

YSP cytotoxicity was evaluated using CCK-8 assay. Magnetic YSPs possessing an outer shell mass ratio (MNP:PCL) of 75 mg/g were sterilized under UV light. 100 μl of uniform cell suspension was seeded in 96-well plates and incubated with YSPs at two selected concentrations (1 and 5 mg/ml) for designated time intervals (1, 2, 4, 8 and 24 h). Seeded cells containing no particulate samples were maintained as control. The culture medium was subsequently removed and 100 μl of CCK-8 solution (1:10 diluted by MEM) was added to each well and incubated for a further 3 h at 37 °C. The optical density (OD) of each well (at 450 nm) was recorded on a microplate reader (VersaMax, Molecular Devices, USA). Cell viability results were presented as the average cell viability $[(OD_{sample} - OD_{blank})/(OD_{control} - OD_{blank}) \times 100\%]$ of quadruplicate wells.

3. RESULTS AND DISCUSSION

3.1. Synthesis of magnetic yolk-shell particles

Synthesis of magnetic YSPs was achieved *via* tri-needle coaxial electrospray setup as shown in **Figure 1a**. Formulated media were infused into outer, central and inner capillaries at flow rates of 10, 2.5 and 1.6 ml/h, respectively. Under co-flowing conditions (all three formulations infused continously) with application (and increments) of voltage field strength, typical transitions of liquid deformation at an electrospraying nozzle exit are observed. In this instance, four jetting modes are encountered: dripping mode, coning mode, stable cone-jet mode and multi-jet mode[24]. The stable cone-jet mode is optimal and is ideal for near-uniform YSP production with intact shell morhology and a well-defined interior structure (obtained at ~10 kV) as shown in **Figure 1b**. **Figure 1c** shows YSP formulation, architecture and compartments. Three media were infused into the tri-needle coaxial nozzle and stable jetting was observed.

Interestingly, the compound jet comprised polymer solutions at inner and outer flows; sandwiching the oil in the central layer compartment. The jetting stability was reminiscent to those osberved for single and conventional two-needle coaxial electrosprays. This indicated YSPs would possess near uniform structures with neat core-shell encapsulation.

3.2. Particle structure and morphology

The external morphology and interior arrangement of YSPs were assessed comprehensively. **Figure 3a** shows optical micrographs of YSPs, which demonstrate a near-uniform size distribution and the inset in **Figure 3a** eludes to the multi-compartment strucutre (i.e. particle in particle). A merged bright field and fluorescent YSP image is shown in **Figure 3b**. Particles consist of a polymeric core, an oily interfacing layer (silicone oil) labeled with Nile red, and a polymeric outer shell, and the overall strucure is well-defined with the central component hosting probe only. Electron micrograph in **Figure 3c** shows YSPs to be spherical possessing a smooth surface shell and this also confirms neat layered encapsualtion of MNPs. **Figure 3d** further indicates the co-flow engineering process was stable, as YSPs possess near uniform size distribtiion (mean diameter=13.5±1.74 μm). The electron micrograph shown as **Figure 3e** highlights a ruptured YSP which may have arisen due to sporadic MNP agglomeration which impedes polymer layering ability during processing on the micron scale. This, however, confirmed the anticipated yolk-shell structure (particle in particle) as evidenced in the micrograph. **Figure 3f** is an electron micrograph showing the cross section of a YSP embedded in epoxy resin. In this instance, the core shell merged with the epoxy resin and the void space between the core and the outer shell indicates the existence of the interfacing oily layer. YSP morphology for samples assessed in air and PBS at 1, 3, 5 and 7 days, respectively, is shown in

Figure 3g. The shape and surface morphology of YSPs show negligible change over 7 days, for both environments, indicating acceptable stability.

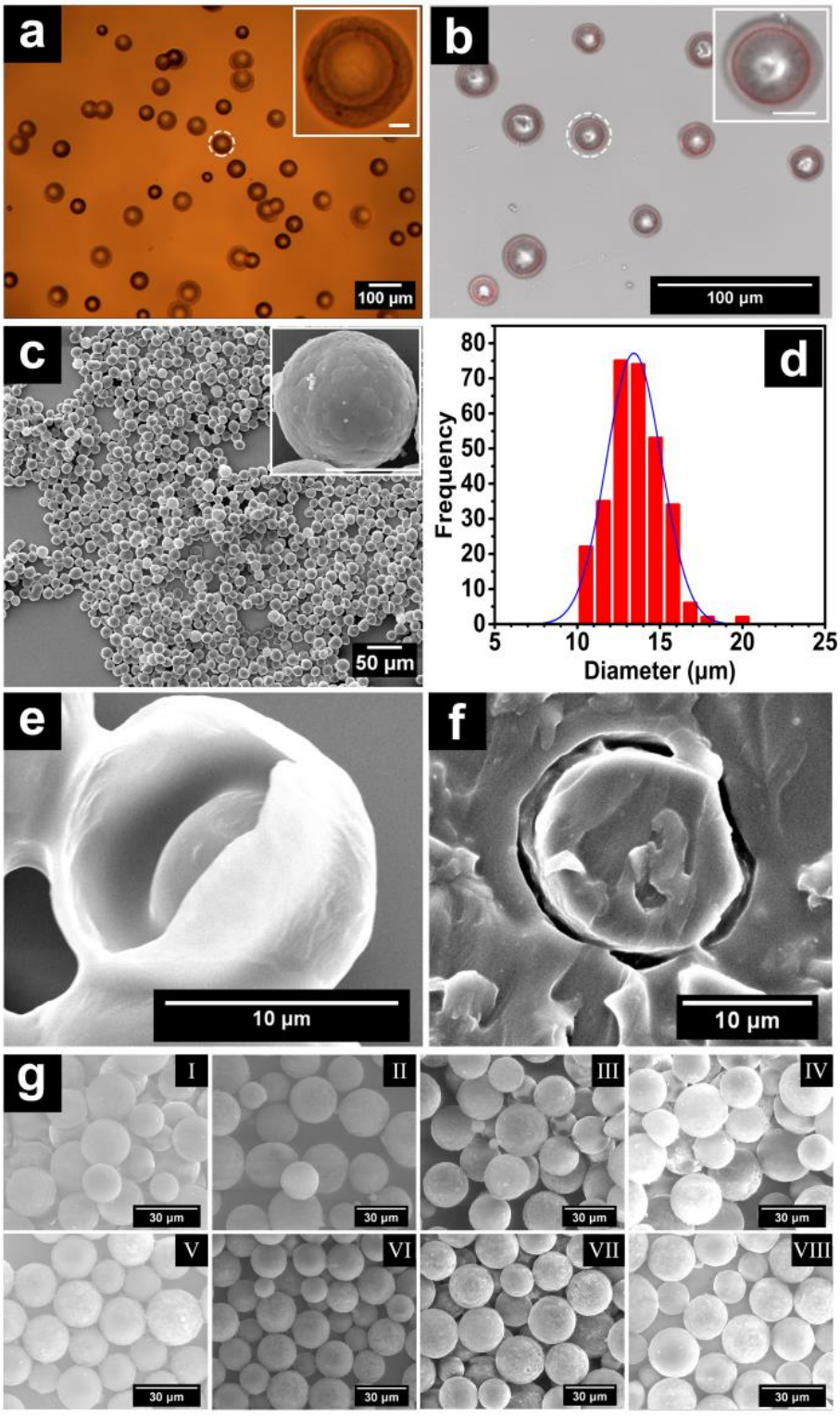

Figure 3. Morphological characterization of yolk-shell particles. (a) Optical micrographs (b) Merged bright-field and fluorescent image of yolk shell particles with the interfacing layer labeled with Nile red. (c) electron micrographs of yolk shell particles and (d) size distribution based on statistical analysis of 300 particles (e) electron micrograph of ruptured micro-particle (f) Cross-section electron micrograph of microsphere embedded in epoxy resin. [scale bar in (c) =10 μm]. (g) electron micrographs of yolk-shell particles in air for 1, 3, 5 and 7 days (I-IV, sequentially) and in PBS for 1, 3, 5 and 7 days (V-VIII, sequentially). [scale bar in (g) =30 μm]

3.3. Chemical composition of yolk shell particles

FTIR spectroscopy was used to confirm the composition of several formulated YSPs (**Figure 4a-d)** and the spectra of pure MNPs and model probes is shown in **Figure 4e-h**. MNP presence is confirmed by the peak at 1551 cm^{-1} (**Figure 4e**) and by comparing spectra for magnetic (**Figure 4c**) and non-magneitc (**Figure 4d**) YSPs; loading of the funcitonal material is confirmed. Characteristic peaks of NB (**Figure 4f**) and AY (**Figure 4g**) are identified in multi-probe loaded YSP samples (**Figure 4a**) at 2362 and 3739 cm^{-1}, respectively. The characteristic peak for probe SRG (**Figure 4h**) is identified in SRG-loaded YSPs at 1185 cm^{-1}. The presence of all formulation components was confirmed, suggesting the tri-needle co-axial electrospying to be viable for multi-material composite engineering and inclusion in a single-step at the ambient environment.

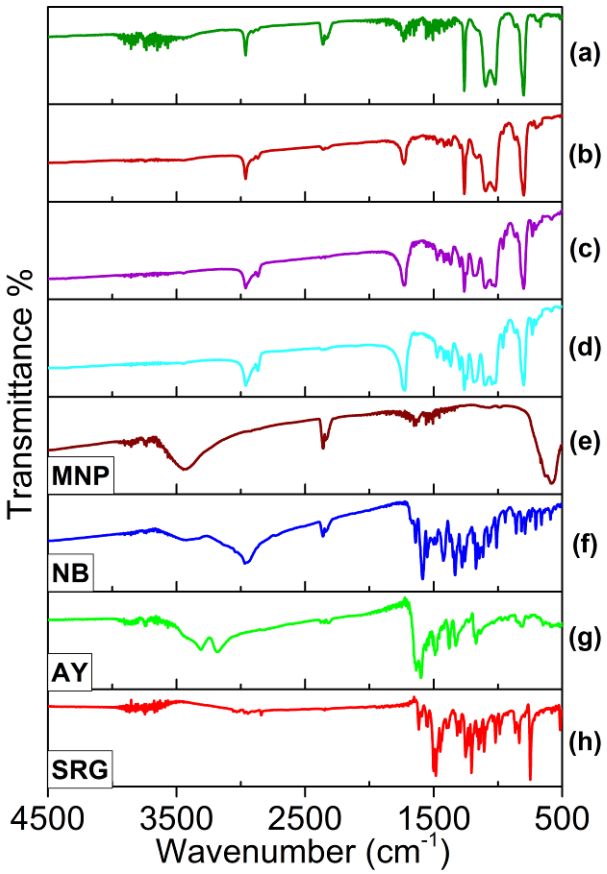

Figure 4. FTIR spectrum of (a) NB and AY loaded magnetic yolk-shell particles, (b) SRG loaded magnetic yolk-shell particles, (c) Magnetic yolk-shell particles, (d) yolk-shell particles without MNPs (e) Pure MNP powder, (f) Pure NB powder, (g) Pure AY powder and (h) Pure SRG powder.

3.4. Magnetic properties

XRD was used to confirm successful encapsualtion of MNPs in YSPs. **Figure 5(a)** shows the XRD spectra of magnetic YSPs with MNP:shell concentration ratio of 75 mg/g. The diffraction peaks for MNPs (2θ angle) at 30.1, 35.5, 43.1, 57.0, 62.6 are indexed as (220), (311), (400), (511) and (440) diffraction plane, respectively, which match well with the values of the standard card (JCPDS card 79-0419)[30] , indicating the incorporation of MNPs in YSPs.

Figure 5(b) shows hysteresis loops for magnetic YSPs prepared with varying MNP: shell concentration ratios (25, 50, 75 mg/g). Corresponding saturation magnetization values were 1.426, 2.918 and 4.263 emu/g, respectively. Saturation magnetization correlated with MNP content in the outer shell (noted as: 1:2:3), which indicates magnetic properties of YSPs can be enhanced directly by increasing functional nano-material content during multi-needle electrospraying. Hysteresis loops show negligible coercivity and remanence magnetization which further indicates MNPs are generally dispersed within the shell thus forming a single domain[31]. Magnetic properties of YSPs were further confirmed by applying a strong magnet to a vial hosting the engineered samples as a suspension (NB-AY loaded YSPs in PBS release medium with 0.5 w/v% SDS) (**Figure 5(b), inset**). With no applied magnetic source (middle vial), YSPs sediment to the base of the vial after several minutes due to their density (1.0710 g/cm^3) being greater than the release medium (1.0099 g/cm^3). The sedimentation of particles causes some agglomeration doe to the hydrophobic nature of PCL polymer. Upon application, particulate samples migrated rapidly towards the magnetic source forming a cluster. This provides a relatively quicker method to separate particles from dissolved/diffused active in test medium (i.e. compared to high speed centrifugation and precipitation, which may also potentially lead to an increase in release from the carrier system[32]). Furthermore, the ability to move and direct YSPs, using a small yet powerful magnet, indicates clear potential for localised drug delivery and targeting.

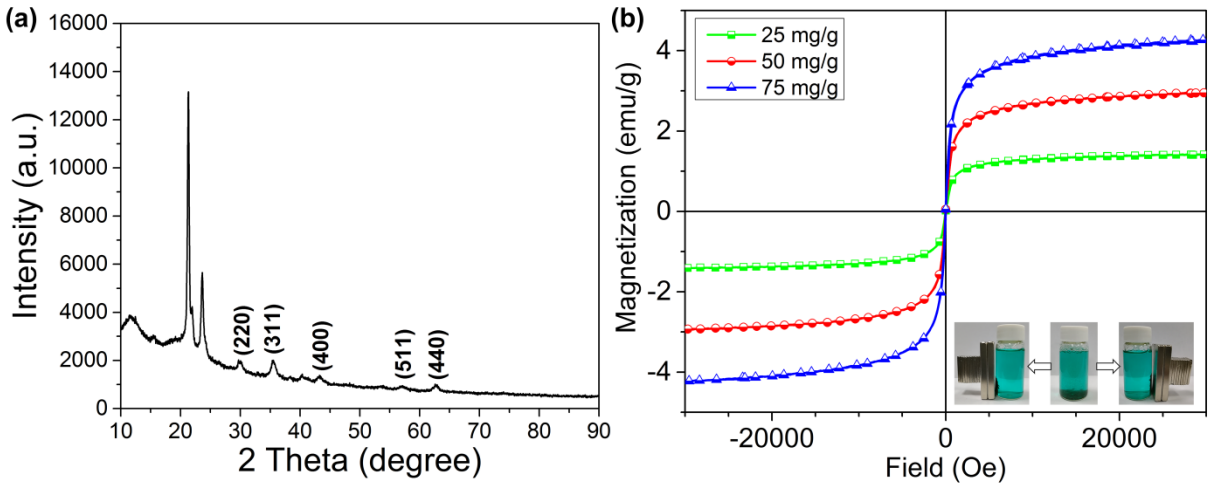

Figure 5. (a) XRD spectra of the magnetic YSPs. (b) Magnetization curves of yolk-shell particles with varying MNP loading content in the outer layer (the legend indicates outer shell mass ratio of MNP:PCL). Inset shows a digital image of particle displacement using a small external magnet.

3.5. *In-vitro* MRI evaluation

To evaluate YSP potential as an MRI contrast agent, a series of agarose phantoms were prepared. Two main factors were investigated. In the first instance, different quantites of YSPs (0.5, 1, 2 and 4 mg) were assessed. The second set focused on varying shell MNP:PCL mass ratios (0, 25, 50, 75 mg/g). For both cases, YSPs were fabricated and both quantitative MRI T_1- and T_2-mapping were explored. Furthermore, MRI T_1- and T_2-weighted images were also measured.

Figure 6a shows T_1 maps (rows 1-2) and T_1-weighted images (rows 3-4), while **Figure 6d** shows T_2 maps (rows 1-2) and T_2-weighted images (rows 3-4). The signal intensity increased with an increase in MNP content (from 0 to 75 mg/g) or sample quantity for T_1-weighted images. Signal intensity decreased with an increase in MNP content (from 0 to 75 mg/g) or sample quantity for T_2-weighted images. **Figure 6b** and **c** indicate that T_1 relaxation time decreases as

MNP content (shell mass ratio, MNP:PCL) or the quantity of magnetic YSP samples is increased. Both trends show a good linear fit, which demonstrates encapsulated MNPs shorten T_1 relaxation time. **Figure 6e** and **f** suggest that MNPs also reduce T_2 relaxation time, which is more notable than the impact on T_1 with curves exhbiting a good linear fit. The results show magnetic YSPs have clear potential as contrast agents for both T_1 and T_2 MRI imaging.

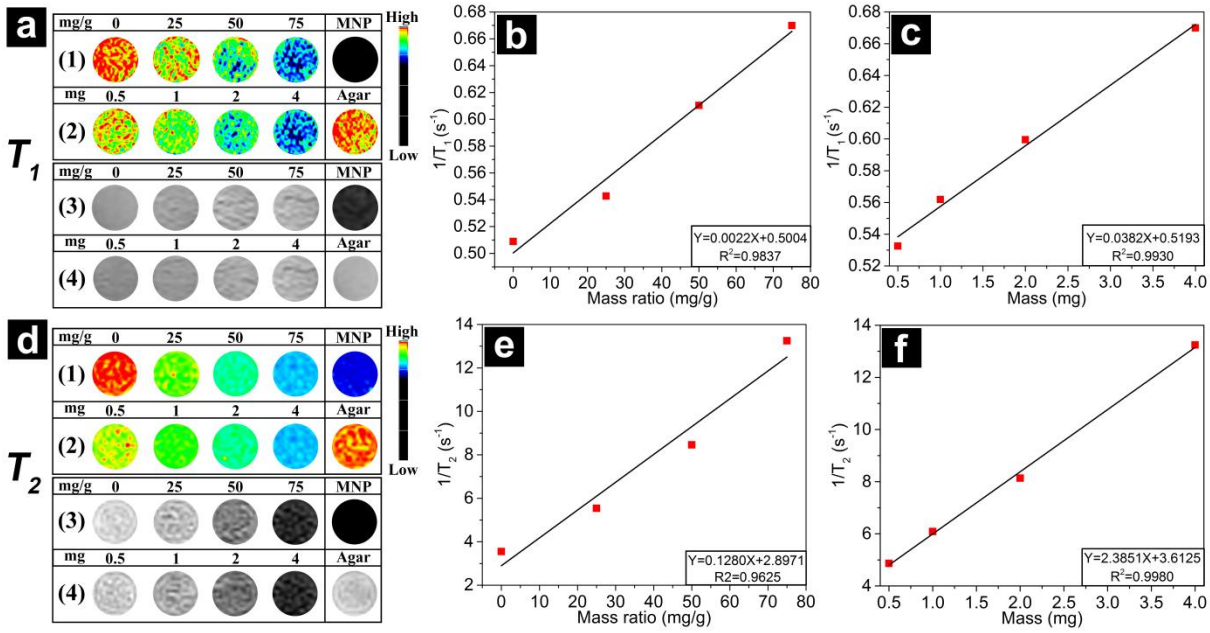

Figure 6. *In vitro* MRI data (a) T_1 maps (rows (1) to (2)) and T_1-weighted MRI images (rows (3) to (4)). (b) and (c) are linear fits of $1/T_1$for phantoms comprising 4 mg of particle samples with varying MNP:PCL shell ratios and varying overall particle quantities using a shell MNP:PCL ratio of 75 mg/g. (d) T_2 maps (row (1) to (2)) and T2-weighted images (row (3) to (4)). (e) and (f) are linear fits of $1/T_2$ for phantoms comprising 4 mg of samples with varying shell MNP: PCL ratios and particle quantities (using a fixed shell MNP:PCL ratio of 75 mg/g).

3.6. *In vitro* acoustic characterization

To evaluate YSP potential as an US contrast agent, acoustic properties of magnetic YSPs (75 mg/g MNP:PCL ratio in the outer shell) at various concentrations (0, 2 and 10 mg/ml) were measured using experimental setup illustrated in **Figure 2**. The frequency spectra demonstrates acoustic performance is enhanced by increasing YSP concentration in the test sample near the centre frequency, as shown in **Figure 7**. Here, ethanol was used as the test medium instead of PBS (or ultrapure water) because of improved YSP dispersibility in the solvent compared to other media.[27]

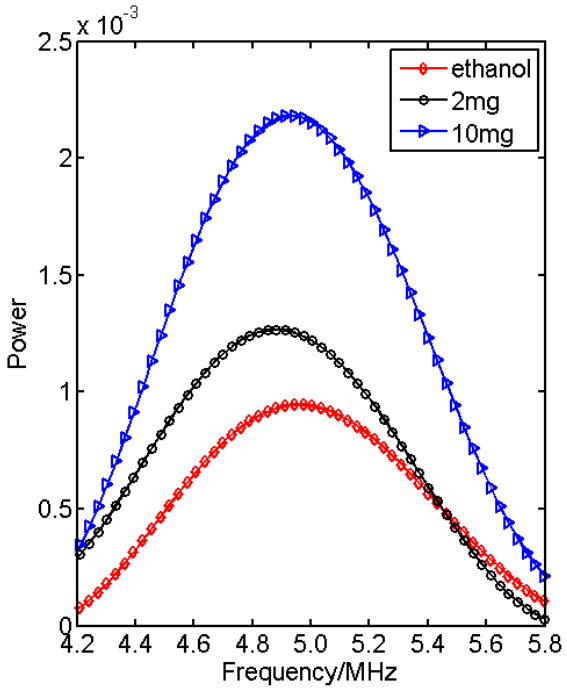

Figure 7. Echo signal frequency spectra of suspensions with varying particle loading volumes in ethanol.

3.7. Multiple *in-vitro* probe loading and release from various particle compartments

The probe loading capacities (LC) of NB, SRG and AY are 0.272 %, 0.078 % and 0.073 %, respectively. The encapsulation efficiencies (EE) of NB, SRG and AY are 88.6 %, 79.3 % and

92.1 %, respectively. Independent release profiles of multiple probes (selected as model agents) from magnetic YSPs were comprehensively studied. Over the last two decades, explorations into synergistic chemotherapies (utilizing two or more actives) to treat various types of cancers have broadened, and numerous efforts have focused on the role and development of advanced carriers systems.[17-18, 33-34] For drug carrier design; hydrophilicity of incorporated active is a crucial factor, not only for matrix dispersibility but to achieve ideal therapeutic release.[16, 35] Therefore, development of advanced carrier systems capable of delivering active(s) with varying hydrophilicities is extremely valuable. In addition to delivery, a process which enables encapsulation of a broad range of chemical agents is also desirable due to formulation barriers.

In order to demonstrate hydrophobic and hydrophilic agent encapsulation; single-step co-encapsulation (and subsequent co-delivery) from a single carrier was demonstrated. NB and AY probes were selected as model hydrophilic agents and SRG was chosen as the hydrophobic component. To ensure accuracy for release measurments (overcoming any issues arising from key overlapping characteristic peaks), NB & AY probe loaded YSPs (and SRG loaded YSPs) were fabricated independently. For NB and AY co-loading, NB was dispersed into the outer polymeric shell and AY was incorporated in to the inner core. For SRG loading into YSPs, the compound was mixed with SLO in the interfacing oily layer, as a single agent delivery system.

A schematic illustration and corresponding UV-vis spectra from the two deployed samples is shown in **Figure 8a** and **b**. The spectrum in **Figure 8a** shows the maximum absorption peaks of NB and AY, which were identified at 637 and 460 nm, respectively. **Figure 8b** shows the maximum absorption peak of SRG (509 nm) which exhibits a relatively high absorption range (350 to 650 nm); and this shoulders peaks for NB and AY. Standard calibration curves for

various probes (NB, AY and SRG) are shown in **Figure 8c-e**. A good linearity and fit for data points was achieved ensuring release kinetic readings were reliable and accurate.

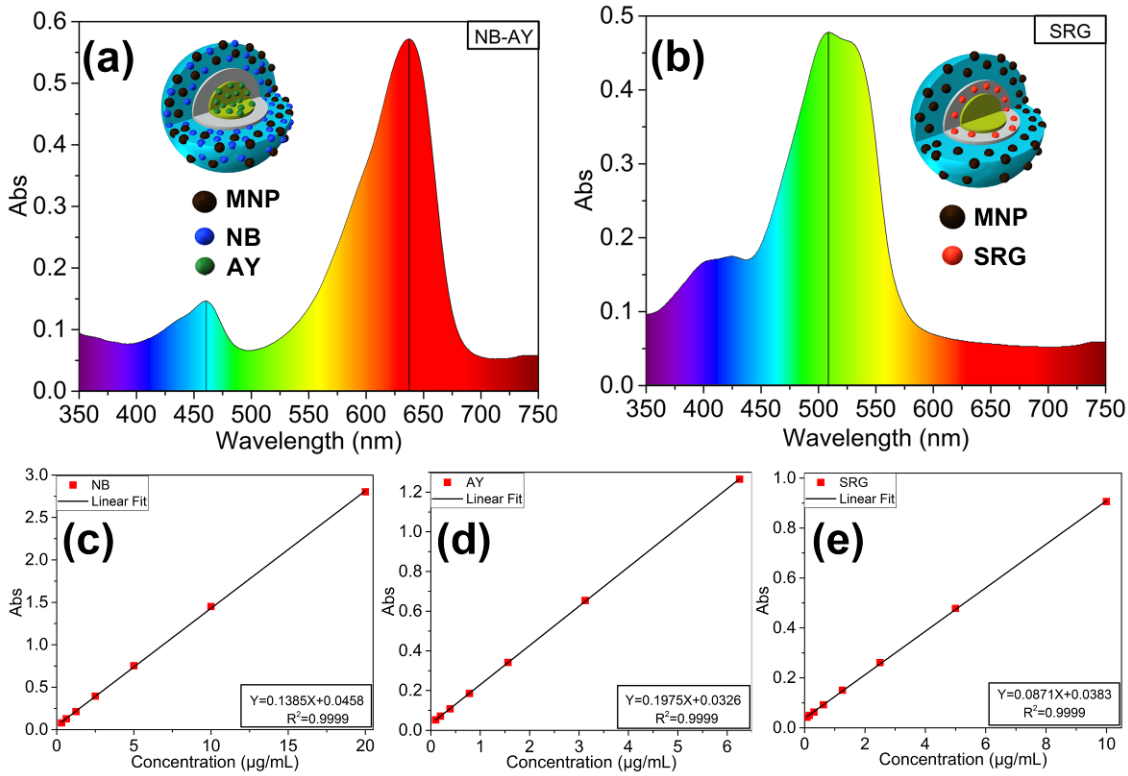

Figure 8. Graphic representations of yolk-shell particles and corresponding UV-vis spectra of probe hosting supernatants obtained from release medium (a) NB-AY and (b) SRG. (c), (d) and (e) are standard calibration curves for probes NB, AY and SRG at their maximum absorption peak values (637.5, 460.5 and 509 nm, respectively).

Probe release profiles over a 7 day period at ambient temperature (23.5 °C) and under static condition's (control, no AMF trigger) are displayed in **Figure 9a**. NB displayed the most rapid release rate in the first 12 h (84.6%) and greatest final release quantity (97.8%) after 7 days. Quantities of AY and SRG released were 64.1 and 53.1%, respectively, at the first 12 h and the total final released quantity of these compounds were 86.1 and 64.9%, respectively. The

relatively low release rate of SRG is attributed to its high solubility in SLO and poor solubility in the aqueous release medium, which retained a considerable portion of the probe (35.1%) in YSPs post 7 days assessemement.

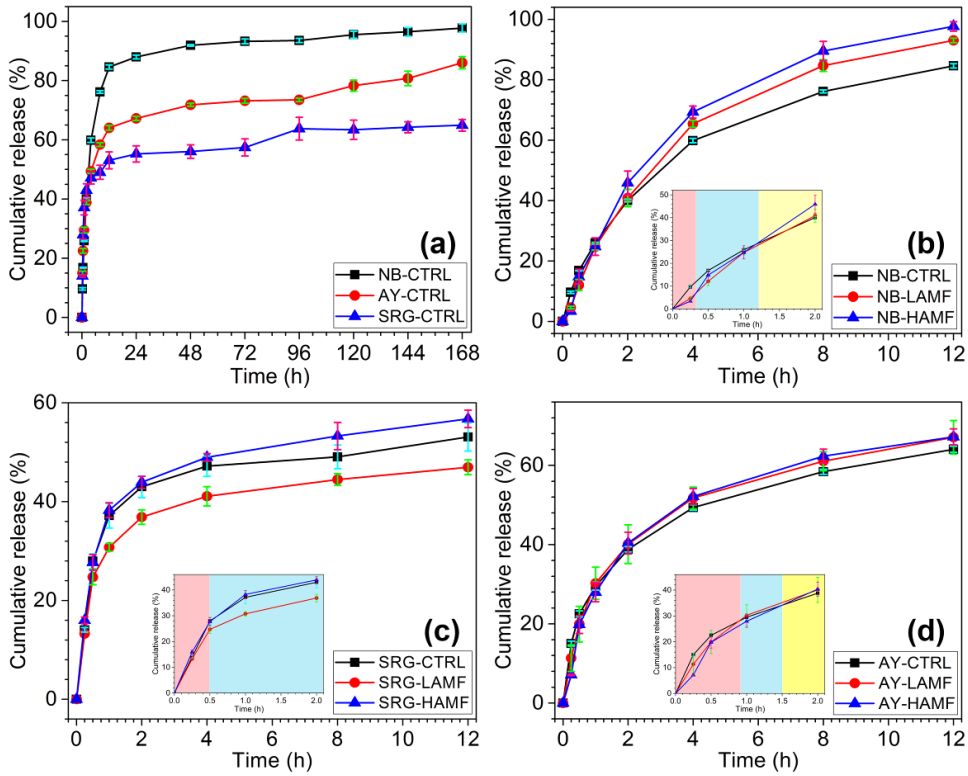

Figure 9. Cumulative probe release profiles with and without AMF exposure (a) Long-term release of probe (for seven days) without AMF (control group). (b), (c) and (d) comparison of probe release (NB, SRG and AY, respectively) without AMF (CTRL) and with external AMF at low (LAMF) and high (HAMF) power for 12 h. Insets in (b)-(d) show magnified views of data points between 0~2 h, and designated release stages are highlighted in different colours.

Figure 9b, **c** and **d** show release behavior of NB, SRG and AY probes under the infleunce of an external AMF using two power settings (LAMF: 0.7 mT and HAMF: 1.4 mT) at 40 kHz, respectively. The release of both hydrophilic compounds, NB (**Figure 9b**) and AY (**Figure 9d**),

is enhanced compared to the control group when magnetic YSPs are exposed to an external AMF. This is attributed to AMF interaction with co-encapsulated MNPs, which produces heat due to hysteresis, Néel and Brownian relaxation upon exposure to AMF[36]. In addiiton, probe release is more pronounced when the higher AMF power setting is deployed (HAMF, 1.4 mT). For hydrophobic probe (SRG, **Figure 9c**) the greaest release rate is observed at the HAMF. However, the lowest SRG release rate was obtained using low power AMF setting (LAMF, 0.7 mT); and was more sustained than the control group (no AMF trigger deployed). It is interesting to note that SRG release behavior is different to other probes under an AMF, with contrasting hydrophillicities (e.g. NB and AY). AMF action leads to magnetic YSP compression and exertion against the particle shells surface, which in turn impacts adjacent YSPs.[32] In this regard, for oil-phase compartment, the volume of encapsulated central medium is "locked" in the YSP structure and inhibited from direct contact with the surface. Therefore, although the temperature of intra-particle oil-phase may increase moderately (from 23.5 to 28.0 °C) upon exposure to LAMF, the release of hydrophobic probe is actually impeded by micron-scaled barrier function.

In addition, magnetic compression induced "inversion", which is defined here as reduced drug release rate phenomenon upon AMF application, was observed and is highlighted in **Figure 9b-d insets**. The inset background color indicates different release phases for each probe in the first 2 h, with variations arising to phases based on test parameters. As represented, particles in the HAMF group do not always exhibit fastest probe release rates. Likewise YSPs in the control group do not release probe at the slowest rate; indicating probe release cannot be confined to a single law in general. At initial release study stages (< 2 h), probe release from all non-triggered YSP specimens is greater than outcomes observed for both LAMF and HAMF treated samples. At intermediate phases, probe release rate from LAMF and HAMF triggered groups become

comparable to non-triggered samples. In general, multiple-probe release from magnetic YSPs is a complicated process governed by several mechanisms (e.g. dissolution, diffusion and AMF induced effects). The interesting "inversion" aspect, which is often missed due to the enhanced active release impact from temperature rise, is observed at LAMF and is documented in this study.

Data obtained for multi-probe release kinetics were fitted to the Korsmeyer-Peppas model to determine potential release mechanisms. The model is expressed as shown in **Equation 3**.[37]

$$M_t/M_\infty = kt^n \quad (3)$$

Here, M_t/M_∞ is the fraction released drug at time t, k is the release rate constant, and n is the release exponent. In this model, the value of n is used to postulate the release mechanism. For a spherical matrix, $n \leq 0.43$ corresponds to Fickian diffusion, $0.43 < n < 0.85$ to anomalous transport, $n = 0.85$ to case II (relaxational) transport, and $n > 0.85$ to super case II transport. Data were plotted as log cumulative percentage drug release versus log time for the first 4 h of probe release (the fraction of released probe ranged from 45 to 65%). The fitting parameters obtained from Korsmeyer-Peppas model are displayed in **Table 1**.

Table 1

Fitting parameters for probe release from yolk shape particles.

Drug-Mode	Korsmeyer-Peppas Model		
	Equation	n	R^2
NB-CTRL	log(Mt/M∞*100)=0.2436+0.6510*log(t)	0.6510	0.9962
NB-LAMF	log(Mt/M∞*100)=-0.3625+0.9423*log(t)	0.9423	0.9750
NB-HAMF	log(Mt/M∞*100)=-0.6928+1.1066*log(t)	1.1066	0.9675
AY-CTRL	log(Mt/M∞*100)=0.6134+0.4872*log(t)	0.4872	0.9868
AY-LAMF	log(Mt/M∞*100)=0.4721+0.5389*log(t)	0.5389	0.9708
AY-HAMF	log(Mt/M∞*100)=0.1815+0.6764*log(t)	0.6764	0.9150
SRG-CTRL	log(Mt/M∞*100)=0.3517+0.7015*log(t)	0.7015	0.9456
SRG-LAMF	log(Mt/M∞*100)=0.4399+0.6058*log(t)	0.6058	0.9289
SRG-HAMF	log(Mt/M∞*100)=0.4775+0.6309*log(t)	0.6309	0.9778

According to fitting parameters, only NB-LAMF and NB-HAMF probe release profiles follow super case II transport, while all other release kinetics indicate anomalous transport.[38] This difference is attributed to co-disperion of NB and MNPs within the same YSP layer (compartment). Upon application of an external AMF (to YSPs), heat production from magnetic energy dissipation as Brown and Néel relaxations, mechanical vibration and motion induces stress in the shell layer of YSPs. The impact of these relaxations and other heat induced effects result in alteration to the polymeric shell microstructure.[39] In contrast, although AY and SRG probes are also affected by generated heat, resulting stress towards the shell is lower due to encapsulation in non-MNP compartments. The impact of varying AMF frequencies (20, 40 and

80kHz) on probe release profiles were also investigated to further confirm "inversion" aspects in the first 2 h (**Figure 10a-c**). NB and AY probes exhibit "inversion" phenomena at 20, 40 and 80 kHz, while this was only present at 20 KHz for SRG. The finding indicates the "inversion" is a universal mechanism regardless of probe hydrophilicity. The real time *in-situ* temperature of particulate samples exposed to HAMF is shown in **Figure 10d**. Thermal graphs demonstrate near identical temperatures for all release media hosting various YSP samples. The temperature increases rapidly during the first 2 h (23.5 to 31 °C) and then a gradual increment is observed, eventually reaching 33 °C over the next 4 h. This confirmed MNPs induce heat upon exposure to AMF, which is an important factor in enhancing model probe release.

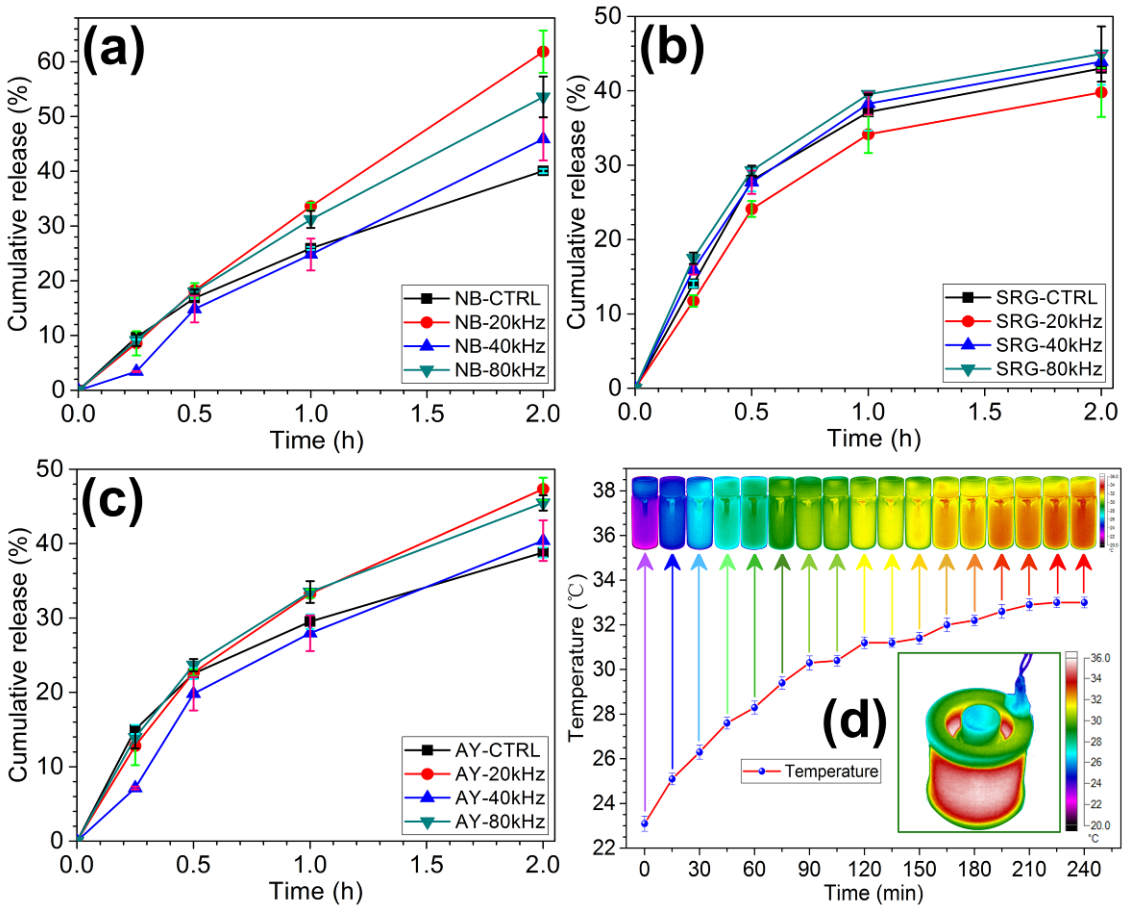

Figure 10. Cumulative release profiles of model probes with external AMF at varying frequencies. (a), (b) and (c) are probe release profiles with (20kHz, 40kHz and 80kHz) and without AMF (CTRL) (d) shows thermally imaged temperature-variation curve of selected sample vials over 4 h. Inset shows the setup used for the release process treated with external AMF.

3.8. Cell culture and fluorescent microscopy

To assess biocompatibility, cells were incubated with YSPs for 24 h at various concentrations (0, 1 and 5 mg/ml). For this YSPs possessing a shell MNP:PCL ratio of 75 mg/g MNPs were fixed and counterstained using DAPI for nuclei and rhodamine–phalloidin for cytoskeleton. Fluorescent images are shown in **Figure 11**, which indicate negligible cytotoxicity. Probe loaded YSPs were not assessed due to their fluoresecing nature and their well documented toxicity.

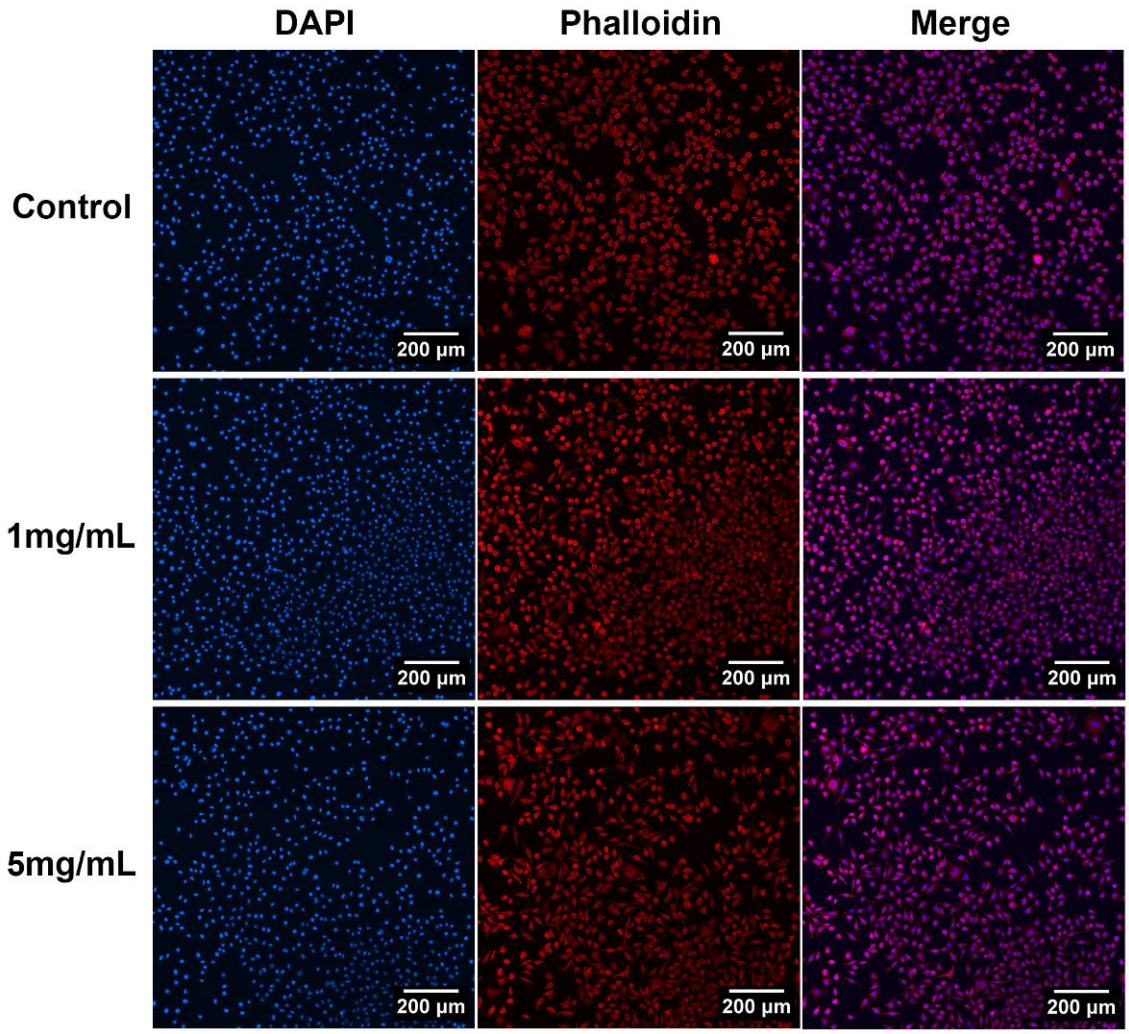

Figure 11. Cells incubated with yolk-shell particle samples at varying concentrations over 24 h. Figures in left and central columns are fluorescent micrographs of nuclei stained with DAPI (blue) and cytoskeleton stained with rhodamine-phalloidin (red). Merged images are shown in the right column.

3.9. Cell viability

Cells incubated with YSP samples (using various particle concentrations and incubation times) were quantitatively assessed using CCK-8 assay. As shown in **Figure 12**, YSPs exihibit negligible toxicity toward cells and a slight improvement in cell viability at 4, 8 and 24 h

incubation times was observed when compared to the control group (culture medium alone), indicating excellent biocompatibility. However, at an incubation time of 24 h, cell viability at a concetraion of 5 mg/ml is lower than 1 mg/ml. This is ascribed to degradation of PCL into toxic ε-caproic acid.[40]

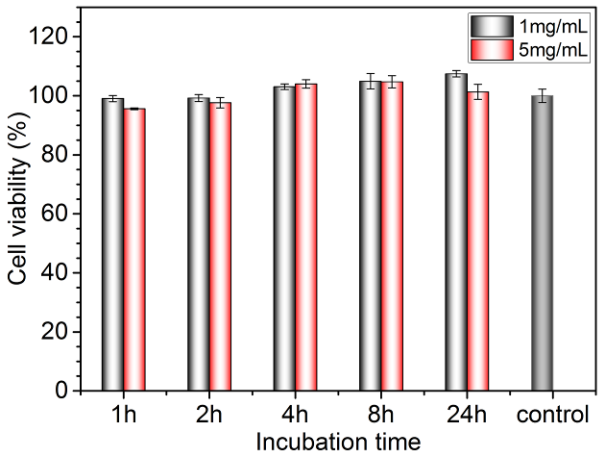

Figure 12. Cell viability with varying quantities of magnetic yolk-shell particles over designated time periods.

4. CONCLUSIONS

In summary, multiple probe hosting magnetic YSPs were successfully synthesized *via* tri-needle coaxial electrospraying. The surface morphology and interior structure of YSPs were demonstrated using fluorescent, optical and scanning electron microscopy. Magnetic properties and chemical composition of YSPs were confirmed by VSM and FTIR, respectively. *In-vitro* MRI/US dual-imaging modality and AMF triggered controlled release (for both hydrophilic and hydrophobic probes) were demonstrated. YSPs exhibit clear potential as synergistic micron-scaled platforms for theranostic applications. Cytotoxic experiments confirmed acceptable biocompatibility. Finally, in addition to their structural design, the facile engineering process is

valuable for sensitive active pharmaceutical ingredients where product forming is required, ideally, in a single step at ambient environments.

AUTHOR INFORMATION

Corresponding Author

*Email: mwchang@zju.edu.cn. Tel.: +86 (0)571-87951517. Fax: +86 (0)571-87951517.

Author Contributions

The manuscript was written through contributions of all authors. All authors have given approval to the final version of the manuscript.

Notes

The authors declare no competing financial interest.

ACKNOWLEDGMENT

The authors would like to thank Prof. Jianhui Zhong for his valuable suggestions and technical guidance in the preparation of this manuscript. This work was financially supported by the National Nature Science Foundation of China (No. 81301304), the Key Technologies R&D Program of Zhejiang Province (2015C02035) and the Fundamental Research Funds for the Central Universities (2017QNA5017).

REFERENCES

(1) Deng, H.; Dai, F.; Ma, G.; Zhang, X., Theranostic Gold Nanomicelles made from Biocompatible Comb‐like Polymers for Thermochemotherapy and Multifunctional Imaging with Rapid Clearance. *Adv. Mater.* **2015,** *27* (24), 3645-3653.
(2) Mignot, A.; Truillet, C.; Lux, F.; Sancey, L.; Louis, C.; Denat, F.; Boschetti, F.; Bocher, L.; Gloter, A.; Stéphan, O.; Antoine, R.; Dugourd, P.; Luneau, D.; Novitchi, G.; Figueiredo, L. C.; de Morais, P. C.; Bonneviot, L.; Albela, B.; Ribot, F.; Van Lokeren, L.; Déchamps‐Olivier, I.;

Chuburu, F.; Lemercier, G.; Villiers, C.; Marche, P. N.; Le Duc, G.; Roux, S.; Tillement, O.; Perriat, P., A Top‐Down Synthesis Route to Ultrasmall Multifunctional Gd‐Based Silica Nanoparticles for Theranostic Applications. *Chem.-Eur. J.* **2013,** *19* (19), 6122-6136.
(3) Yoon, Y. I.; Kwon, Y. S.; Cho, H. S.; Heo, S. H.; Park, K. S.; Park, S. G.; Lee, S. H.; Hwang, S. I.; Kim, Y. I.; Jae, H. J., Ultrasound-mediated gene and drug delivery using a microbubble-liposome particle system. *Theranostics* **2014,** *4* (11), 1133-1144.
(4) Janib, S. M.; Moses, A. S.; Mackay, J. A., Imaging and drug delivery using theranostic nanoparticles. *Adv. Drug Del. Rev.* **2010,** *62* (11), 1052-1063.
(5) Xie, J.; Lee, S.; Chen, X., Nanoparticle-based theranostic agents. *Adv. Drug Del. Rev.* **2010,** *62* (11), 1064-1079.
(6) Cavalli, R.; Argenziano, M.; Vigna, E.; Giustetto, P.; Torres, E.; Aime, S.; Terreno, E., Preparation and in vitro characterization of chitosan nanobubbles as theranostic agents. *Colloids Surf., B* **2015,** *129*, 39-46.
(7) Jiao, Y.; Sun, Y.; Tang, X.; Ren, Q.; Yang, W., Tumor-targeting multifunctional rattle-type theranostic nanoparticles for MRI/NIRF bimodal imaging and delivery of hydrophobic drugs. *Small* **2015,** *11* (16), 1962-1974.
(8) Lee, N.; Yoo, D.; Ling, D.; Cho, M. H.; Hyeon, T.; Cheon, J., Iron oxide based nanoparticles for multimodal imaging and magnetoresponsive therapy. *Chem. Rev.* **2015,** *115* (19), 10637-10689.
(9) Yang, F.; Li, Y.; Chen, Z.; Zhang, Y.; Wu, J.; Gu, N., Superparamagnetic iron oxide nanoparticle-embedded encapsulated microbubbles as dual contrast agents of magnetic resonance and ultrasound imaging. *Biomaterials* **2009,** *30* (23–24), 3882-3890.
(10) Liao, Z.; Wang, X.; Wang, C.; Wang, H.; Hu, X.; Cao, X.; Chang, J., Biocompatible surfactin-stabilized superparamagnetic iron oxide nanoparticles as contrast agents for magnetic resonance imaging. *Colloids Surf., A* **2010,** *370* (1), 1-5.
(11) Wang, X.; Tu, M. Q.; Yan, K.; Li, P. H.; Pang, L.; Gong, Y.; Li, Q.; Liu, R. Q.; Xu, Z. S.; Xu, H. B.; Chu, P. K., Trifunctional Polymeric Nanocomposites Incorporated with Fe3O4/Iodine-Containing Rare Earth Complex for Computed X-ray Tomography, Magnetic Resonance, and Optical Imaging. *ACS Appl. Mater. Interfaces* **2015,** *7* (44), 24523-24532.
(12) Gao, Y.; Chang, M. W.; Ahmad, Z.; Li, J. S., Magnetic-responsive microparticles with customized porosity for drug delivery. *RSC Adv.* **2016,** *6* (91), 88157-88167.
(13) Malvindi, M. A.; Greco, A.; Conversano, F.; Figuerola, A.; Corti, M.; Bonora, M.; Lascialfari, A.; Doumari, H. A.; Moscardini, M.; Cingolani, R., Magnetic/silica nanocomposites as dual-mode contrast agents for combined magnetic resonance imaging and ultrasonography. *Adv. Funct. Mater.* **2011,** *21* (13), 2548-2555.
(14) D'Arrigo, G.; Navarro, G.; Di Meo, C.; Matricardi, P.; Torchilin, V., Gellan gum nanohydrogel containing anti-inflammatory and anti-cancer drugs: a multi-drug delivery system for a combination therapy in cancer treatment. *Eur. J. Pharm. Biopharm.* **2014,** *87* (1), 208-216.
(15) Parhi, P.; Mohanty, C.; Sahoo, S. K., Nanotechnology-based combinational drug delivery: an emerging approach for cancer therapy. *Drug Discov. Today* **2012,** *17* (17–18), 1044-1052.
(16) Nii, T.; Ishii, F., Encapsulation efficiency of water-soluble and insoluble drugs in liposomes prepared by the microencapsulation vesicle method. *Int. J. Pharm.* **2005,** *298* (1), 198-205.
(17) Narayanan, S.; Pavithran, M.; Viswanath, A.; Narayanan, D.; Mohan, C. C.; Manzoor, K.; Menon, D., Sequentially releasing dual-drug-loaded PLGA-casein core/shell nanomedicine: design, synthesis, biocompatibility and pharmacokinetics. *Acta Biomater.* **2014,** *10* (5), 2112-2124.

(18) Shin, H.-C.; Alani, A. W. G.; Rao, D. A.; Rockich, N. C.; Kwon, G. S., Multi-drug loaded polymeric micelles for simultaneous delivery of poorly soluble anticancer drugs. *J. Controlled Release* **2009,** *140* (3), 294-300.
(19) Cao, Y.; Wang, B.; Wang, Y.; Lou, D., Dual drug release from core–shell nanoparticles with distinct release profiles. *J. Pharm. Sci.* **2014,** *103* (10), 3205-3216.
(20) Lee, Y.-H.; Bai, M.-Y.; Chen, D.-R., Multidrug encapsulation by coaxial tri-capillary electrospray. *Colloids Surf., B* **2011,** *82* (1), 104-110.
(21) Hu, S. H.; Chen, Y. Y.; Liu, T. C.; Tung, T. H.; Liu, D. M.; Chen, S. Y., Remotely nano-rupturable yolk/shell capsules for magnetically-triggered drug release. *Chem. Commun.* **2011,** *47* (6), 1776-1778.
(22) Fang, Q.; Xuan, S.; Jiang, W.; Gong, X., Yolk‐like Micro/Nanoparticles with Superparamagnetic Iron Oxide Cores and Hierarchical Nickel Silicate Shells. *Adv. Funct. Mater.* **2011,** *21* (10), 1902-1909.
(23) Liu, J.; Qiao, S. Z.; Chen, J. S.; Lou, X. W.; Xing, X.; Lu, G. Q., Yolk/shell nanoparticles: new platforms for nanoreactors, drug delivery and lithium-ion batteries. *Chem. Commun.* **2011,** *47* (47), 12578-12591.
(24) Yuan, G.; Ding, Z.; Chang, M. W.; Ahmad, Z.; Li, J. S., Optimising the shell thickness-to-radius ratio for the fabrication of oil-encapsulated polymeric microspheres. *Chem. Eng. J.* **2015,** *284*, 963–971.
(25) Yao, Z. C.; Gao, Y.; Chang, M. W.; Ahmad, Z.; Li, J. S., Regulating poly-caprolactone fiber characteristics in-situ during one-step coaxial electrospinning via enveloping liquids. *Mater. Lett.* **2016,** *183*, 202-206.
(26) Cui, F.; Yang, M.; Jiang, Y.; Cun, D.; Lin, W.; Fan, Y.; Kawashima, Y., Design of sustained-release nitrendipine microspheres having solid dispersion structure by quasi-emulsion solvent diffusion method. *J. Controlled Release* **2003,** *91* (3), 375-384.
(27) Zhang, H.; Tong, S.-Y.; Zhang, X.-Z.; Cheng, S.-X.; Zhuo, R.-X.; Li, H., Novel solvent-free methods for fabrication of nano- and microsphere drug delivery systems from functional biodegradable polymers. *J. Phys. Chem. C* **2007,** *111* (34), 12681-12685.
(28) Yao, Z. C.; Chang, M. W.; Ahmad, Z.; Li, J. S., Encapsulation of rose hip seed oil into fibrous zein films for ambient and on demand food preservation via coaxial electrospinning. *J. Food Eng.* **2016,** *191*, 115-123.
(29) Deng, P.; Teng, F.; Zhou, F.; Song, Z.; Meng, N.; Feng, R., Methoxy poly (ethylene glycol)-b-poly (δ-valerolactone) copolymeric micelles for improved skin delivery of ketoconazole. *J. Biomater. Sci., Polym. Ed.* **2017,** *28* (1), 63-78.
(30) Zhu, H.; Zhu, L.; Yang, D., Hydrothermal growth and characterization of magnetite (Fe 3O 4) thin films. *Surf. Coat. Technol.* **2007,** *201* (12), 5870-5874.
(31) Song, S.; Guo, H.; Jiang, Z.; Jin, Y.; Wu, Y.; An, X.; Zhang, Z.; Sun, K.; Dou, H., Self-assembled microbubbles as contrast agents for ultrasound/magnetic resonance dual-modality imaging. *Acta Biomater.* **2015,** *24*, 266-278.
(32) Hu, Y.; Liu, C.; Li, D.; Long, Y.; Song, K.; Tung, C. H., Magnetic compression of polyelectrolyte microcapsules for controlled release. *Langmuir* **2015,** *31* (41), 11195-11199.
(33) Wei, L.; Cai, C.; Lin, J.; Chen, T., Dual-drug delivery system based on hydrogel/micelle composites. *Biomaterials* **2009,** *30* (13), 2606-2613.
(34) Dilnawaz, F.; Singh, A.; Mohanty, C.; Sahoo, S. K., Dual drug loaded superparamagnetic iron oxide nanoparticles for targeted cancer therapy. *Biomaterials* **2010,** *31* (13), 3694-3706.

(35) Gurny, R.; Doelker, E.; Peppas, N. A., Modelling of sustained release of water-soluble drugs from porous, hydrophobic polymers. *Biomaterials* **1982,** *3* (1), 27-32.
(36) Hawkins, A. M.; Bottom, C. E.; Liang, Z.; Puleo, D. A.; Hilt, J. Z., Magnetic nanocomposite sol-gel systems for remote controlled drug release. *Adv. Healthcare Mater.* **2012,** *1* (1), 96-100.
(37) Korsmeyer, R. W.; Gurny, R.; Doelker, E.; Buri, P.; Peppas, N. A., Mechanisms of solute release from porous hydrophilic polymers. *Int. J. Pharm.* **1983,** *15* (1), 25-35.
(38) Peppas, N. A.; Sahlin, J. J., A simple equation for the description of solute release. III. Coupling of diffusion and relaxation. *Int. J. Pharm.* **1989,** *57* (2), 169-172.
(39) Hu, S. H.; Tsai, C. H.; Liao, C. F.; Liu, D. M.; Chen, S. Y., Controlled rupture of magnetic polyelectrolyte microcapsules for drug delivery. *Langmuir* **2008,** *24* (20), 11811-11818.
(40) Taylor, M. S.; Daniels, A. U.; Andriano, K. P.; Heller, J., Six bioabsorbable polymers: In vitro acute toxicity of accumulated degradation products. *J. Appl. Biomater.* **1994,** *5* (2), 151-157.

TOC FIGURE

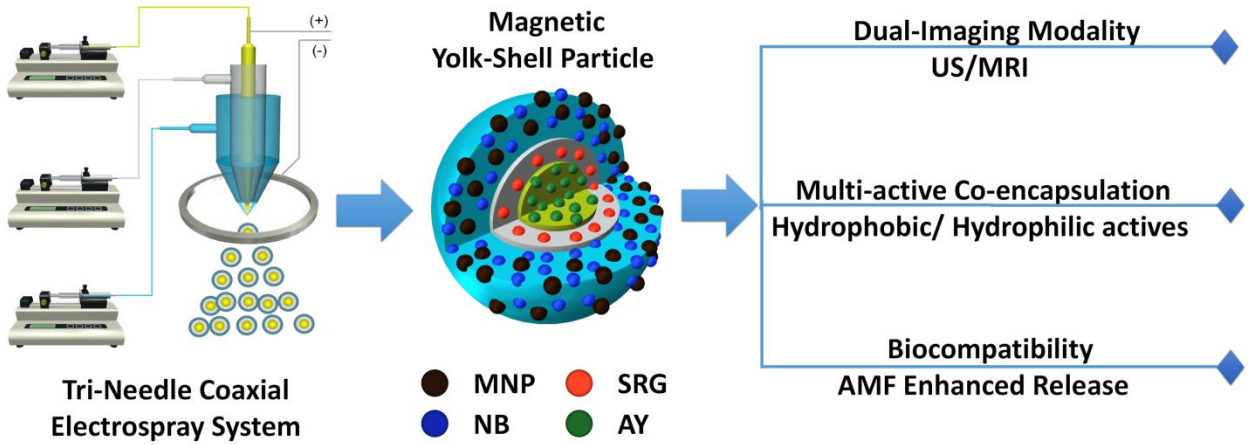
(+)
(-)
Tri-Needle Coaxial
Electrospray System
Magnetic
Yolk-Shell Particle
MNP
SRG
NB
AY
Dual-Imaging Modality
US/MRI
Multi-active Co-encapsulation
Hydrophobic/ Hydrophilic actives
Biocompatibility
AMF Enhanced Release